Measuring ^{1}H–^{1}H and ^{1}H–^{13}C RDCs in methyl groups: example of pulse sequences with numerically optimized coherence transfer schemes

Konstantin Pervushin*, Beat Vögeli, Tim N. Heinz, Philippe H. Hünenberger

Laboratory of Physical Chemistry, Swiss Federal Institute of Technology, ETH-Hönggerberg, CH-8093 Zürich, Switzerland

Received 27 August 2004; revised 27 August 2004

Abstract

The optimization of coherence-transfer pulse-sequence elements (CTEs) is the most challenging step in the construction of heteronuclear correlation NMR experiments achieving sensitivity close to its theoretical maximum (in the absence of relaxation) in the shortest possible experimental time and featuring active suppression of undesired signals. As reported in the present article, this complex optimization problem in a space of high dimensionality turns out to be numerically tractable. Based on the application of molecular dynamics in the space of pulse-sequence variables, a general method is proposed for constructing optimized CTEs capable of transferring an arbitrary (generally non-Hermitian) spin operator encoding the chemical shift of heteronuclear spins to an arbitrary spin operator suitable for signal detection. The CTEs constructed in this way are evaluated against benchmarks provided by the theoretical unitary bound for coherence transfer and the minimal required transfer time (when available). This approach is used to design a set of NMR experiments enabling direct and selective observation of individual ^{1}H-transitions in ^{13}C-labeled methyl spin systems close to optimal sensitivity and using a minimal number of spectra. As an illustrative application of the method, optimized CTEs are used to quantitatively measure ^{1}H–^{1}H and ^{1}H–^{13}C residual dipolar couplings (RDCs) in a 17 kDa protein weakly aligned by means of Pf1 phages.
© 2004 Elsevier Inc. All rights reserved.

Keywords: Coherence and polarization transfer; Molecular dynamics; Simulated annealing; Optimization of NMR experiments; Methyl groups; TROSY

1. Introduction

The design of a particular NMR experiment is dictated by the type of spectral information desired. For complex spin systems in large biomolecules, specific experiments may be exceptionally difficult to construct when high sensitivity, suppression of spurious signals, and tolerance to relaxation effects are required. For example, ^{13}C-labeled methyl groups represent one of the most complicated systems of *J*-coupled homo- and heteronuclear spins found in solvated proteins and nucleotides. Previously an experiment recovering individual ^{1}H transitions was proposed to measure ^{1}H–^{1}H residual dipolar couplings in methyl groups [1]. Although proven to be practically useful this experiment does not deliver theoretically possible sensitivity and the time duration of its critical coherence transfer element (CTE) was not evaluated against theoretical benchmarks. A general tool enabling constructing of coherence transfer- and pulse-sequence duration-optimized complex NMR experiments especially in applications to methyl groups would enable, e.g., (i) the enhancement of the resolution in TROSY-based experiments [2–5]; (ii) the investigation of the spin dynamics associated with the fast rotation of methyl groups in proteins with high

---
* Corresponding author. Fax: +4116321021.
  E-mail address: kope@phys.chem.ethz.ch (K. Pervushin).

molecular weights [6]; (iii) the direct measurement of cross-correlations between Curie spin relaxation and ^{1}H–^{1}H dipole–dipole relaxation within methyl groups of paramagnetic proteins [7–14]; (iv) the measurement of the absolute values and signs of residual ^{1}H–^{1}H (D_{HH}) and ^{1}H–^{13}C (D_{HC}) dipolar couplings [15–17] within methyl groups of proteins that are weakly aligned in solution [18–20].

Heteronuclear chemical shift correlation experiments typically rely on several types of basic building blocks [21,22]. These include a polarization transfer element (PTE), followed by an element indirectly encoding the chemical shifts of the heteronuclear spins (CSE), and a coherence transfer element (CTE) providing a density operator suitable for signal detection. The PTE and CSE elements can be combined into a so-called coherence excitation element (CEE). Several attempts have been made to systematically optimize these elements based on analytical or numerical approaches. For example, a spin-state selective PTE was optimized for the presence of residual dipolar couplings using a target-function minimization algorithm [23]. The theoretical upper bound for the PTE efficiency in a two spin-1/2 system subjected to relaxation was established [24,25], and experimentally feasible PTEs were proposed to drive the density operator along the theoretically optimal pathway. An example of optimized CSE is the TROSY experiment (transverse relaxation optimization) [2]. Efforts have also been dedicated to the optimization of CTEs [26–31], resulting in a significant enhancement of the spectral sensitivity. The upper bound for an arbitrary coherence transfer [32–34] and the minimal time required to accomplish this transfer (the latter only for special cases) [35–37] were established analytically, providing very useful benchmarks for further optimizations of the CTEs involved in specific experiments.

In this article, we present an approach suitable for systematic construction of CTEs capable of transferring an arbitrary (generally non-Hermitian) operator A encoding the chemical shift of heteronuclear spins to another arbitrary operator C suitable for signal detection in methyl groups. The maximization of the efficiency for this transfer is undertaken simultaneously with the minimization of the pulse-sequence duration (to avoid problems related to relaxation) and of the transfer to an operator D (or to a set of such operators) representing undesired or spurious signals in the spectrum. This formulation translates into a complex optimization problem in a space of high dimensionality, the degrees of freedom being the pulse-sequence variables (pulse flip angles and phases, as well as delays between pulses) defining the CTE. As an example, we selected a problem of measuring ^{1}H–^{1}H and ^{1}H–^{13}C RDCs in methyl groups. However, although complex, this problem is tractable numerically because all components of the above optimization statement (efficiency of the desired

transfer, suppression of undesired transfers, and pulse-sequence duration) can be translated into computationally tractable mathematical functions. Due to the availability of analytical gradients for these functions, methods like gradient-based function minimization (e.g., steepest descent) or molecular dynamics [38] (e.g., simulated annealing [39]) can be applied to find a near-optimal solution to this problem.

The performance of CTEs constructed using this approach is evaluated against the benchmarks provided by the theoretical unitary bound for coherence transfer [33] and the corresponding minimal transfer time (when available) [35].

2. Theoretical part

2.1. Heteronuclear coherence transfer in I_3S spin systems

The present discussion is restricted to the I_3S spin system, where I_3 denotes three magnetically equivalent spin-1/2 entities I (e.g., ^{1}H) and S a heteronuclear spin (e.g., ^{13}C), coupled via a scalar coupling constant J_{IS}. This situation represents one of the most difficult spin systems encountered, e.g., for the methyl groups in biomolecules. However, the present formalism is easily extended to other spin systems (e.g., I_2S in methylene groups or systems of coupled ^{13}C and ^{1}H homonuclear spins). The spins of type I are combined for convenience into a pseudospin $F = I^{(1)} + I^{(2)} + I^{(3)}$. It is also assumed that the coherence transfer is achieved by a sequence of unitary transformations neglecting the effect of relaxation and involving non-selective radiofrequency (RF) pulses.

The aim of the method is to maximize a coherence transfer $A \to C$, while simultaneously minimizing an undesired transfer $A \to D$ and the pulse-sequence duration Θ, based on experimentally accessible propagators U resulting from the generic CTEs shown in Figs. 1C and D. The source operators A considered here will be restricted to

$$A_1 = 2F_z S^- \quad \text{and} \quad A_2 = (F_x S^-)_{\alpha\beta} + (F_x S^-)_{\beta\alpha}. \tag{1}$$

In terms of the individual spins, the latter operator may be rewritten as $A_2 = I_x^{(1)} S^- (E - 4I_z^{(2)}I_z^{(3)}) + I_x^{(2)} S^- (E - 4I_z^{(1)}I_z^{(3)}) + I_x^{(3)} S^- (E - 4I_z^{(1)}I_z^{(2)})$, where E is the identity operator. These two operators, used to record the chemical shift of the spin S, can be generated by the CEEs displayed in Figs. 1A and B. These are transferred to the target operators

$$C_1 = F_{\alpha\alpha\alpha}^- + F_{\beta\beta\beta}^- \quad \text{and} \quad C_2 = F_{\alpha\alpha\beta}^- + F_{\beta\beta\alpha}^-, \tag{2}$$

while the corresponding suppressed-target operators are

$$D_1 = F_{\alpha\beta\alpha}^- + F_{\beta\alpha\alpha}^- + F_{\alpha\beta\beta}^- + F_{\beta\alpha\beta}^- + F_{\alpha\alpha\beta}^- + F_{\beta\beta\alpha}^- \tag{3a}$$
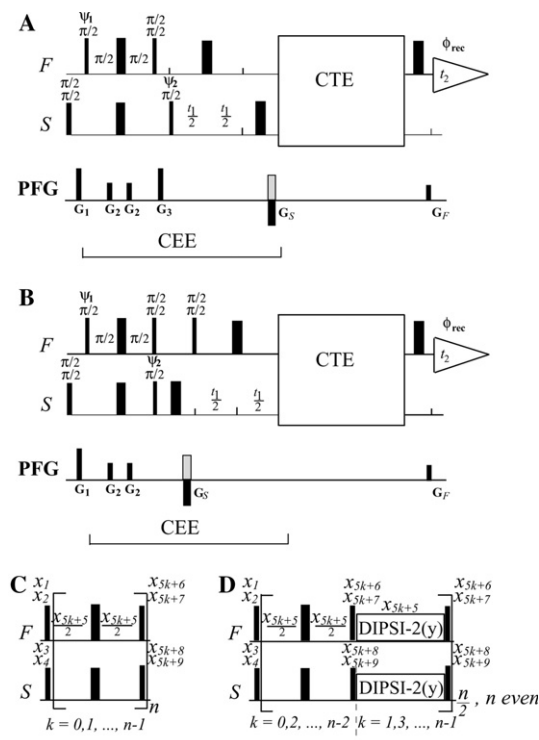
Fig. 1. General pulse sequences of two-dimensional $[I_N, S]$-correlation experiments for spin systems consisting of N magnetically equivalent spin-1/2 entities $I^{(i)}$, $i = 1,\ldots,N$, coupled to a heteronuclear spin S by the coupling constant J_{IS}. For convenience, the spins I are combined into a pseudospin $F_k = \sum_i^N I_k^{(i)}$, where $k \in \{x,y,z\}$. In (A and B), an excitation of the coherences $2F_zS_x$ and $2F_xS_x$, respectively, is performed and used for chemical-shift encoding of the spin S. The sequences consist of a coherence excitation (CEE) element followed by a coherence transfer element (CTE). Two types of CTEs, based either on a sequence of n pulse-interrupted free precession (INEPT) elements, or an alternating sequence of n INEPT and planar-mixing elements, are shown in (C) and (D), respectively. Wide black bars indicate non-selective π RF-pulses applied with the zero phase corresponding to the x-axis, according to the usual notation for the direction of the oscillating magnetic field in the rotating frame [45]. In this notation, the phases $\pi/2$, π, and $3\pi/2$ rad correspond to the y-, x-, and $-y$-axes, respectively. Narrow black bars indicate arbitrary non-selective RF-pulses characterized by the phase (first row) and the flip angle (second row) indicated above the bar. The planar mixing sequence consists of a DIPSI-2 pulse train applied with the phase $\pi/2$ simultaneously to both the F and S channels. The length ϕ of the free-precession delays and planar-mixing sequences is given in radian, and is related to the metric time τ according to the equation $\phi = 2\pi J_{IS}\tau$. The pulses and delays in square brackets are repeated n times (C) or $n/2$ times with n even (D). Thus, CTE of either type is entirely defined by a vector x of variables x_i (in radian), with $i = 1, 2, \ldots, 5n+4$. In the present work, when applied to $[^{13}C, {}^1H]$-correlation experiments on methyl groups, the RF-pulses on the ^{13}C (spin S) and ^1H (spin I) nuclei are centered at 20 and 3 ppm, respectively. In this case the durations and strengths of the pulsed magnetic field gradients (PFG) applied along the z-axis are selected as G_1: 800 μs, 80 G/cm; G_2: 800 μs, 20 G/cm; G_3: 1 ms, −60 G/cm; G_S: 1 ms, 90 G/cm; G_F 251 μs, 90 G/cm. A uniform value of $J_{CH} = 125$ Hz is assumed for all methyl groups to determine the actual duration of the free-precession delays and planar-mixing sequences. The phases in (A) and (B) are defined as: $\psi_1 = \{x, -x\}$; $\psi_2 = \{2y, 2(-y)\}$; $\phi_{rec} = \{x, -x, -x, x\}$. Quadrature detection in the $^{13}C(t_1)$-dimension is achieved by the echo–anti-echo method [26,51]. The anti-echo signal is obtained by inversion of the phase x_3 in the CTE, with simultaneous inversion of the sign of the G_S pulse.

and

$$D_2 = F_{\alpha\beta\alpha}^- + F_{\beta\alpha\alpha}^- + F_{\alpha\beta\beta}^- + F_{\beta\alpha\beta}^- + F_{\alpha\alpha\alpha}^- + F_{\beta\beta\beta}^-. \tag{3b}$$

In the above equations, the subscript triplets $i,j,k \in \{\alpha, \beta\}$ designate the spin states of the ^1H, ^1H, and ^{13}C spins (in this order). The pseudospin operators can be rewritten in terms of the individual spin operators as, $F_{\alpha\alpha\alpha/\beta\beta\beta}^- = I^{(1)-}(E \pm 2I_z^{(2)})(E \pm 2I_z^{(3)})(E \pm 2S_z) +$ two isomorphous terms with circularly permuted indexes 1, 2, and 3, where the state α in a given position of the subscript list maps to the "+" sign in the corresponding position of the right-hand side. A spectral representation of individual spin transitions is provided in Fig. 2A. The choice of the specific operators in Eqs. (1), (2), and (3a) will be discussed in Section 3.

The operators defined above, as well as the unitary-transformation propagator U resulting from an experimentally accessible CTE, can be represented as matrices in a basis conforming with the symmetry properties of the spin system [40,41]. In the case of the I_3S system,
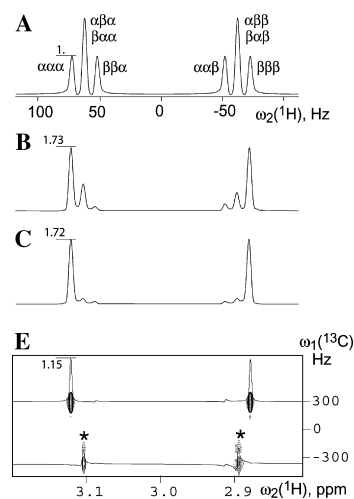

Fig. 2. Simulated two-dimensional $[^{13}C, {}^1H]$-correlation spectra (and corresponding one-dimensional ^1H-slices) for a methyl group with $\omega(^{13}C) = 300$ Hz, $\omega(^1H) = 3$ ppm, $J_{CH} = 125$ Hz, and $D_{HH} = 10$ Hz. The spectra were calculated using the program NMRSIM (Bruker AG). (A) Slice at $\omega_1(^{13}C) = 300$ Hz of a $[^{13}C, {}^1H]$-sensitivity-enhanced HSQC spectrum [51] calculated without ^{13}C-decoupling during signal acquisition. The individual components of the ^1H-multiplet detected via $I^{(1)-}$ are designated according to the state of the spins $I^{(2)}$, $I^{(3)}$ and S. (B and C) Slices at $\omega_1(^{13}C) = 300$ Hz of the $[^{13}C, {}^1H]$-correlation spectra calculated using the experimental scheme of Fig. 1A based on OCTE$_1$ and OCTE$_2$ (Table 1), respectively. The inner components ($\beta\beta\alpha$ and $\alpha\alpha\beta$) of the ^1H-multiplet can be obtained by repeating the calculations with inversion of the phases of the first pulse on the channel S and the last pulse on the channel F of CTE, together with the inversion of the sign of G_S. (D) Contour plot of the $[^{13}C, {}^1H]$-correlation spectrum superimposed with slices at $\omega_1(^{13}C) = 300$ and -310 Hz, calculated using the experimental scheme of Fig. 1B, based on OCTE$_3$ (Table 1) and the strength of both G_S and G_F set to zero. The signals designated by asterisks can be suppressed using non zero values of G_S and G_F. All one-dimensional slices are drawn to the scale and the amplitudes relative to the $\alpha\alpha\alpha$ component in (A) are explicitly indicated.

the corresponding matrices A, C, D, and U assume a block structure along the diagonal, consisting of one square block of dimensions 8×8 and 2 identical square blocks of dimensions 4×4, as shown in Fig. 3. Since, in the absence of relaxation, there is no "cross-talk" between individual blocks, it is sufficient to consider the unitary transformations separately for the 8×8 and one of the 4×4 blocks [41], thereby reducing dimensionality of the problem.

In the absence of relaxation, the transfer $A \rightarrow C$ can be described by [31]

$$UAU^{\dagger} = b(U)C + Q \text{ with } \text{Tr}\{C^{\dagger}Q\} = 0, \tag{4}$$

where the dagger denotes Hermitian conjugation, Q is a residual operator, and $b(U)$ is the transfer efficiency given by

$$b(U) = \text{Tr}\{UAU^{\dagger}C\}/\text{Tr}\{C^{\dagger}C\}. \tag{5}$$

The maximum value $b_{\max}$ of the complex norm of $b(U)$, the so-called unitary bound value, can be determined numerically for arbitrary source and target operators [33]. This quantity represents an important benchmark for the construction and evaluation of optimized CTEs. It has been demonstrated [34] that in the case of I_3S spin systems with a quantum evolution governed by non-selective RF irradiation and heteronuclear J-coupling Hamiltonians, it is always possible to construct a CTE which achieves the maximum polarization-transfer efficiency $b_{\max}$.

A CTE can be constructed experimentally using either a series of n pulse-interrupted free-precession periods [42] (INEPTs [43,44]), as shown in Fig. 1C, or an alternating series of n INEPT and planar-mixing sequences (the latter usually implemented via the DIPSI-2 supercycle [31]), as shown in Fig. 1D. Since in the I_3S spin-system operators F_kS_k, with $k \in \{x, y, z\}$, do not commute, it is generally not possible to convert a pure INEPT-based CTE to an alternating INEPT/planar-based CTE and vice versa. Thus, both types of CTEs should be tried out in the optimization process. Note, however, that the INEPT-based CTE is easier to implement in practice since it imposes no restriction on the length of the free-precession delays, while short INEPT/planar-based sequences are restricted by the minimal duration of the DIPSI (or any other) supercycle.

The propagator U corresponding to the CTEs of Figs. 1C and D can be constructed using the skew-Hermitian Hamiltonians:

$$\tau H_{\text{RF}} = i\beta_I(\cos(\alpha_I)F_x + \sin(\alpha_I)F_y)$$
$$+ i\beta_S(\cos(\alpha_S)S_x + \sin(\alpha_S)S_y), \tag{6a}$$

$$\tau H_J = i\gamma F_z S_z, \tag{6b}$$

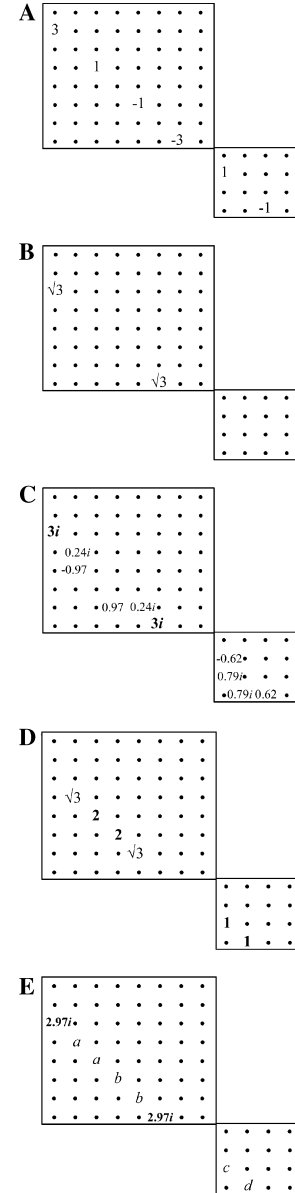$$\tau H_{\text{planar}} = i\gamma/2(F_z S_z + F_x S_x), \tag{6c}$$

Fig. 3. Schematic representation of the matrices associated with specific operators. Examples of matrices are given for (A) the source operator A_1 (Eq. (1)), (B) the target operator $C_1^{\dagger}$, (C) the operator $UA_1U^{\dagger}$ corresponding to the optimized propagator OCTE$_1$ (Table 1), and (D) the operator $D^{\dagger}$ of the suppressed target (Eq. (3a)). (E) The operator $UA_1U^{\dagger}$ corresponding to OCTE$_2$ (Table 1). The actual 16×16 matrices consist of $8 \times 8 + 4 \times 4 + 4 \times 4$ blocks along the diagonal. Only the 8×8 block and one of the two identical 4×4 are displayed. The elements outside the squares are zero. Points in (A, B, and D) represent zero and in (C and E) irrelevant numbers. In (C) the components of the matrix $UA_1U^{\dagger}$ corresponding to the matrix $C_1^{\dagger}$ are highlighted. In (D) the components of the suppression matrix D_1 representing the central transitions of the ^{1}H-multiplet given by the spin operators $F_{\alpha\beta\alpha}^- + F_{\beta\alpha\alpha}^- + F_{\alpha\beta\beta}^- + F_{\beta\alpha\beta}^-$ are shown in bold. In (E) $a = -0.04 - 0.01i$, $b = 0.04 + 0.03i$, $c = -0.21 + 0.10i$, and $d = 0.23 + 0.11i$.

as building blocks. Here, α_I and α_S are the phase shifts of I and S pulses relative to the carrier RF-radiation, $\beta_I = \tau\omega_I^{\text{RF}}$ and $\beta_S = \tau\omega_S^{\text{RF}}$ are the rotation angles (in ra-

dian) of I and S pulses with the strength ω^{RF} and duration τ (defined as in [45]), and $\gamma = 2\pi\tau J_{IS}$. The operator H_{planar} represents the effective approximate planar-mixing Hamiltonian resulting from the DIPSI-2 sequence applied along the y axis. For both INEPT-based and INEPT/planar-based CTEs, the concatenated propagator $U(\boldsymbol{x})$ is a function of a vector $\boldsymbol{x}$ of variables x_i, $i = 1, 2, \ldots, 5n + 4$ containing all the information about the pulse flip angles and phases, the delays between the pulses, and the length of the DIPSI-2 supercycle (see Figs. 1C and D). This vector contains the parameters determining the M individual events (RF-pulse, free precession or planar mixing) in the CTE. The propagator can thus be written

$$U(\boldsymbol{x}) = \prod_{k=1}^{M} \exp(\tau H_k). \tag{7}$$

The quantum evolution of A to C proceeds via infinitely fast rotations under the H_{RF} Hamiltonian (assuming that the RF-pulses are infinitely strong) and the finite-time transformations under the H_{planar} and H_J Hamiltonians. Note that although the events in the pulse sequence of Fig. 1 are represented along time according to a "from-left-to-right" rule, the individual propagators in Eq. (7) are multiplied in the reversed order.

For the numerical optimization of CTEs, it is convenient to define the real and positive target function

$$f_{AC}(\boldsymbol{x}) = b(\boldsymbol{x})b^*(\boldsymbol{x}) \tag{8a}$$

with the short notation $b(\boldsymbol{x}) = b(U(\boldsymbol{x}))$ for the transfer efficiency defined in Eq. (5). The gradient of this function is given by

$$\begin{aligned} \nabla f_{AC}(\boldsymbol{x}) = &(\text{Tr}\{(\nabla U)AU^\dagger C + UA(\nabla U)^\dagger C\}b^*\boldsymbol{x}) \\ &+ b(\boldsymbol{x})(\text{Tr}\{(\nabla U)AU^\dagger C \\ &+ UA(\nabla U)^\dagger C\})^*)/\text{Tr}\{C^\dagger C\}, \end{aligned} \tag{8b}$$

where the star denotes complex conjugation, and ∇U is obtained by applying the chain rule for derivatives to the product in Eq. (7).

As illustrated in Fig. 3C, even in the case of a maximally efficient transformation U of the source operator A (e.g., A_1 in Fig. 3A) to the target operator C (e.g., C_1 in Fig. 3B), the operator Q in Eq. (4) may contain observable magnetization leading to spurious signals in the spectrum. These signals can be combined into the operator D (e.g., D_1 in Fig. 3D), transfer to which can be suppressed by minimizing a function $f_{AD}(\boldsymbol{x})$ analogous to the function $f_{AC}(\boldsymbol{x})$, simultaneously with the maximization of $f_{AC}(\boldsymbol{x})$, itself. However, it turns out that a more efficient reduction of the spurious signals is achieved by suppressing individually a set of matrices $D_i^{(k)}$, $k = 1, \ldots, K$, each containing only one of the K non-zero elements of D_i (e.g., elements $D^{(4,2)}$, $D^{(5,3)}$, $D^{(6,4)}$, $D^{(7,5)}$, $D^{(11,9)}$, $D^{(12,10)}$ in Fig. 3D), because it avoids artificial cancellation of positive and negative contributions to the

penalty function stemming from the different transitions involved in D. In this case, the suppression is achieved by minimizing the sum of functions $f_{AD_k}(x)$, rather than a simple function $f_{AD}(\boldsymbol{x})$, simultaneously with the maximization of $f_{AC}(\boldsymbol{x})$, itself. The matrix representation of the source operator transformed by a unitary propagator optimized through this procedure is given in Fig. 3E.

To complete the specification of the NMR experiment, the matrix $UAU^\dagger$ representing the density operator after the unitary transformation by the CTE is transformed into a detectable spectrum using the free precession Hamiltonian

$$\begin{aligned} H_{obs} = &\text{i}2\pi(({}^1J_{IS} + {}^1D_{IS})F_zS_z + ({}^1J_{II} + {}^1D_{II}) \\ &\times (I_z^{(1)}I_z^{(2)} + I_z^{(1)}I_z^{(3)} + I_z^{(2)}I_z^{(3)})). \end{aligned} \tag{9}$$

The spectrum is then obtained by Fourier transformation of the FID function

$$\text{FID}(t) = \text{Tr}\{\exp(H_{obs}t)C\exp(-H_{obs}t)F^-\}\exp(-Rt), \tag{10}$$

where R is an arbitrary line-broadening parameter. This spectral representation of the target matrix can be used for the direct analysis of the polarization transfer efficiency and of the level of undesired signal suppression achieved by CTE.

2.2. Optimization of the transfer function using molecular dynamics

A CTE composed of a series of n INEPT or n alternating INEPT/planar units (Figs. 1C and D) is entirely defined by the N dimensional vector $\boldsymbol{x}$ introduced above. Given a source matrix A and a number of units n, the problem of simultaneously (i) maximizing the efficiency of transfer to a target matrix C, (ii) minimizing the transfers to a set of suppressed target matrices D_k, $k = 1, \ldots, K$, and (iii) minimizing the pulse-sequence duration may be rewritten in the form of an N-dimensional minimization problem for the target function

$$V(\boldsymbol{x}) = -f_{AC}(\boldsymbol{x}) + \mu\sum_{k=1}^{K} f_{AD}(x) + vg(\boldsymbol{x}), \tag{11}$$

where μ (unitless) and v (units of radian) are weighting coefficients, f_{AC} and f_{AD} are defined by Eq. (8a), and

$$g(x) = \begin{cases} \Theta^2(x) & \text{if } \Theta(x) \leqslant \Theta_0, \\ 2\Theta_0\Theta(x) - \Theta_0^2 & \text{otherwise with } \Theta(x) = \sum_{k=0}^{n-1} x_{5k+5}. \end{cases} \tag{12}$$

The two last terms in Eq. (11) should be viewed as penalty functions imposed during the minimization of the first term. The penalty function associated with the duration Θ of the pulse sequence (sum of delays and DIPSI-2 length variables) is harmonic below a given

threshold Θ_0 and linearized beyond, in such a way that the function is continuous and continuously differentiable over the whole range of durations. The negative gradient $\boldsymbol{F}_i(\boldsymbol{x})$ of $V(\boldsymbol{x})$ is given on a component-by-component basis

$$F_i(x) = -\frac{\partial V(x)}{\partial x_i} = \frac{\partial f_{AC}(x)}{\partial x_i} - \mu \sum_{k=1}^{K} \frac{\partial f_{AD_k}(x)}{\partial x_i} - \nu \frac{\partial g(x)}{\partial x_i}. \tag{13}$$

Because this gradient can be easily calculated (see Eq. (8b)) together with V, one may try to minimize this function by means of a gradient-based function minimization (e.g., steepest descent) algorithm (see Supplementary Material). However, the dimensionality of the problem increases rapidly with the number of INEPTs or alternating INEPT/planar units, while the hypersurface described by V is likely to involve an increasingly larger number of local minima and barriers. For this reason the steepest-descent algorithm, which only leads to the local minimum closest to the given starting point $\boldsymbol{x}(0)$, is not likely to be efficient (i.e., numerous attempts with different random starting points are needed to possibly reach the global minimum). A more efficient strategy is to use a molecular-dynamics (simulated-annealing) algorithm to solve the minimization problem. Speaking of molecular-dynamics is slightly misleading in the present context, because the degrees of freedom involved are not Cartesian coordinates of atoms in molecules, but rather angular variables characterizing a pulse sequence. The term is nevertheless retained here.

In the molecular-dynamics approach, a common "mass" m is assigned to the N degrees of freedom of the problem. These variables are then propagated along a "time" coordinate t according to Newton's second law

$$\mathrm{d}^2\boldsymbol{x}(t)/\mathrm{d}t^2 = \mathrm{d}\boldsymbol{v}/\mathrm{d}t = m^{-1}F(\boldsymbol{x}(t)), \tag{14}$$

where $\boldsymbol{v}$ stands for the "velocity" vector associated with $\boldsymbol{x}$. In this case, V can be interpreted as a "potential energy" to be minimized. In practice, Eq. (14) is integrated iteratively based on a finite time-step size Δt. To enhance the search power of molecular dynamics, the technique of simulated annealing is applied here. In this case, the system is coupled to a thermostat, so that the "kinetic energy" associated to the velocity $\boldsymbol{v}$ (related to a system "temperature"), rather than the total energy, is kept (on average) constant at a specified value. In the simulated-annealing protocol, the imposed value of the kinetic energy is linearly decreased from a large value (efficient crossing of potential energy barriers, search biased towards high-entropy regions) to a small value (poorer search, biased towards low potential energy regions) over the given number of time steps of a run. This search is then followed by a steepest-descent minimization.

All the searches (steepest descent as well as simulated annealing) are carried out under periodic boundary conditions. The pulse flip angle and phase-shift variables in $\boldsymbol{x}$ are restricted to the range $[0, 2\pi]$ by application of 2π-periodicity, while the corresponding delay variables are restricted to the range $[0, 4\pi]$ by application of "mirroring" boundary conditions. The latter choice ensures that the function g in Eq. (11) is continuous throughout the search (periodic boundary conditions would lead to discontinuities in this case).

3. Results and discussion

3.1. Selection of the source, target and suppression operators

Fig. 2A shows a simulated one-dimensional ^{1}H-spectrum of a methyl group of a hypothetical protein slightly aligned in solution (e.g., with residual dipolar coupling $D_{HH} = 10$ Hz). Individual transitions of the multiplet pattern are labeled according to the spin states of the coupled ^{1}H-, ^{1}H-, and ^{13}C-spins involved (in this order). Note that individual transitions involving the magnetically equivalent ^{1}H-spins could not be observed as multiplet-split NMR lines in the absence of alignment ($D_{HH} = 0$ Hz). To measure the value of the D_{HH} coupling constant, the ^{1}H-transitions $\alpha\alpha$ and $\beta\beta$ can be observed individually in separate spectra under conditions of ^{13}C-decoupling [1]. In this case, observation of the $\alpha\alpha\alpha$ and $\beta\beta\beta$ transitions representing the outer components of the ^{1}H-multiplet in one spectrum, and of the $\alpha\alpha\beta$ and $\beta\beta\alpha$ transitions representing the corresponding inner components in the other spectrum, permits the direct estimation of the D_{HH} coupling constant as well as the sum of the D_{HC} and J_{HC} coupling constants.

These considerations result in the choice of the target (detection) operators C_1 and C_2 (Eq. (2)). Note that the insertion of a ^{13}C-π-pulse before signal acquisition in an experiment applying the C_1 operator is equivalent to the application of the C_2, eliminating the need for the separate construction of two complementary experiments. The matrix representation of the target operator C_1 in the symmetry-adapted basis set is shown in Fig. 3B.

To produce a two-dimensional [^{1}H, ^{13}C]-correlation spectrum, a coherence suitable for the detection of the ^{13}C-chemical shifts has to be excited, which will be subsequently transferred (using a suitably constructed CTE) to the target operator for detection. The simplest choice for this source operator is the antiphase operator A_1 (Eq. (1)), which can be easily generated using INEPT [46]. The pulse sequence exciting the coherence associated with the operator A_1 is depicted in Fig. 1A, while the corresponding matrix representation in the symmetry-adapted basis set is shown in Fig. 3A.

A major disadvantage of using the complete anti-phase operator A_1 is its decomposition during the chemical-shift evolution periods, caused by the differential relaxation of the individual transitions comprising the operator [3]. In a coupled heteronuclear single-quantum correlation (HSQC) spectrum, the evolution of A_1 under conditions of negligible relaxation results in four spectral lines with relative intensities 3:1:1:3, comprising eight transitions within the energy-level diagram [4,31]. The transverse magnetization corresponding to the (most intense) outer lines of the quartet relaxes significantly faster than the magnetization associated with the inner ones. As a consequence, the contributions from the outer lines can become quite small in systems of high molecular weight [4]. This relaxation-induced decomposition results in numerous spurious transfers and, therefore, in significantly biased measurements.

In contrast, the coupled heteronuclear multiple-quantum correlation (HMQC) spectrum measured using the $2F_xS^-$ source operator for detection of ^{13}C-chemical shifts exhibits (in the absence of relaxation) only three lines with relative intensities 1:2:1 comprising four transitions. For the two central transitions, dipolar auto- and cross-correlation contributions completely cancel out. This represents a completely optimized TROSY effect, resulting from the combination of fast methyl rotation and very slow overall molecular tumbling [3–6,47]. These TROSY transitions are defined by the operator A_2 (Eq. (1)), which is therefore an attractive source operator for the construction of quantitative NMR experiments. The pulse sequence exciting the coherence associated with the operator A_2 is depicted in Fig. 1B, while the corresponding matrix representation in the symmetry-adapted basis set is shown in Supplementary Material. Note that the exci-

tation of this TROSY operator requires active filtering of the two outer transitions, which otherwise can result in spurious signals. Fortunately, the signals stemming from the undesired outer transitions can be suppressed without introduction of extra delays in the experiment. To achieve this filtering, the experimental scheme of Fig. 1B takes an advantage of the facts that: (i) the operators representing the inner and outer transitions of the triplet evolve with opposite frequencies (see simulated spectrum of Fig. 2D); (ii) the constructed CTE preserves the coherence order (e.g., in one experiment the "minus" source operators are transferred exclusively to "minus" target operators). Therefore, adjusting the signs of the G_S and G_F gradients (see Fig. 1), either the inner or the outer components of the triplet can be refocused (see caption of Fig. 2).

A first attempt to construct a CTE achieving the transfer $A_1 \rightarrow C_1$ with high efficiency by direct maximization of the function f_{AC} (Eq. (8a)) without additional restraints resulted in an alternating INEPT/planar-based CTE with $n = 2$ projecting the source operator on the desired target operator with maximal theoretical efficiency b_{max}. This optimized CTE will be referred as OCTE$_1$. The corresponding parameter vector x is given in Table 1, the matrix representation of the operator $UAU^\dagger$ in Fig. 3C, and the simulated spectrum in Fig. 2B. As can be seen both from the matrix and the spectrum, the undesired multiplet components can reach a magnitude as high as one-third of the signal of interest. This can be particularly inconvenient for practical applications involving high molecular weights, where the unwanted central component of the multiplet is TROSY-enhanced. Therefore it is essential to be able to actively minimize transfers to the undesired transitions.

Table 1
Theoretical maximal bound, b_{max}, relative experimental transfer efficiency b/b_{max}, ratio of the absolute values of amplitudes of the suppressed central $\|a^{\alpha\beta\alpha} + a^{\beta\beta\alpha}\|$ and inner $\|a^{\beta\beta\alpha}\|$ components to the amplitude of the selected $\|a^{\alpha\alpha\alpha}\|$ component of the ^{1}H-multiplet, and the duration Θ of designed coherence transfer elements (CTE)

Type of transfer	b_{max}	b/b_{max} (%)	$\|a^{\alpha\beta\alpha} + a^{\beta\beta\alpha}\|/\|a^{\alpha\alpha\alpha}\|$, $\|a^{\beta\beta\alpha}\|/\|a^{\alpha\alpha\alpha}\|$ (%)	Θ (rad)
$A_1 \rightarrow C_1$ (OCTE$_1$)[a]	$\sqrt{3}$	100	30, 8	3.62
$A_1 \rightarrow C_1$ (OCTE$_2$)[b]	$\sqrt{3}$	98	9, 3	5.09
$A_2 \rightarrow C_1$ (OCTE$_3$)[c]	$\frac{2}{\sqrt{3}}$	90	0, 3	6.73
$A_1 \rightarrow F_{\alpha\alpha}^-$ [1][d]	$\sqrt{3}$	62	0, 0	3.45

[a] The pulse sequence OCTE$_1$ relies on an alternating INEPT/planar sequence with $n = 2$, and was optimized by direct maximization of f_{AC} in Eq. (8a) for the transfer $A_1 \rightarrow C_1$ without additional restraints. The corresponding pulse-sequence vector (Fig. 1E) is $x = \{\pi, \pi/2, 0, \pi/2, 3.62, \pi, \pi/2, \pi, \pi/2, 0, 0, 0, 0\}$. See also the matrix of Fig. 3C and spectrum of Fig. 2B.

[b] The pulse sequence OCTE$_2$ relies on an alternating INEPT/planar sequence with $n = 2$ (Fig. 1E) and was optimized for the transfer $A_1 \rightarrow C_1$ by minimization of V in Eq. (11) with $\Theta_0 = 7$ rad, $\mu = 1$ rad^{-1} and $v = 25$ rad^{-1} through simulated annealing. The corresponding pulse-sequence vector is $x = \{\pi, 3.03, 0, 3\pi/4, 1.93, 0, 1.44, 6.12, 0, \pi, 0, 4.84, \pi, \pi/2\}$. See also the matrix in Fig. 3E and spectrum in Fig. 2C.

[c] The pulse sequence OCTE$_3$ relies on an INEPT sequence with $n = 4$ (Fig. 1D) and was optimized for the transfer $A_2 \rightarrow C_1$ by minimization of V in Eq. (11) with $\Theta_0 = 7$ rad, $\mu = 1$ rad^{-1} and $v = 25$ rad^{-1} through simulated annealing. The corresponding pulse-sequence vector is $x = \{4.66, 4.37, 0.97, 3\pi/4, 1.74, 4.88, 0.20, 0.60, 5.50, 1.81, 0.14, 3.96, 2.54, 4.26, 2.21, 1.17, 2.03, 3.74, 1.97, 0.96, 5.32, 4.59, 0.97, 1.57\}$. See also the matrix in Supplementary Material and spectrum in Fig. 2D.

[d] The detection operator $F_{\alpha\alpha}^- = I^{(1)-}(E + 2I_z^{(2)})(E + I_z^{(3)})$ + two isomorphous terms with circularly permuted indexes 1, 2, and 3 [1].

3.2. Boundaries and criteria of optimization

The theoretical bounds b_{max} characterizing the maximal achievable efficiency for the unitary transformation of the source operator to the target operator were evaluated numerically [33,34], and are listed in Table 1 for the transfers $A_1 \rightarrow C_1$ and $A_2 \rightarrow C_1$. The corresponding bounds for the $A_1 \rightarrow C_2$ and $A_2 \rightarrow C_2$ transfers, respectively, evaluate to the same two values. Analytical estimates Θ_{min} for the minimal pulse sequence length required for the desired coherence transfer are currently only available for a limited set of special cases [35–37]. In the present case, this value is only available for the $A_1 \rightarrow C_1$ transfer ($\Theta_{min} = 3.62$, the proof to be published elsewhere) and it is indeed achieved in the experiment based on $OCTE_1$ (see Table 1). For the transfer of $A_2 \rightarrow C_1$, the analytical minimal transfer time remains to be established.

An important criterion in the construction of practically useful CTEs is their complexity, defined by the number n of repeating units (Fig. 1C) or alternate repeating units (Fig. 1D) they consist of. Direct maximization of the function f_{AC} in Eq. (8a) without additional restraints were performed for INEPT-based CTEs with different levels of complexity n. These results, shown in Fig. 4, suggest that for any transfer $A \rightarrow C$, an optimized CTE capable of reaching the theoretical unitary bounds b_{max} should possess a minimal complexity level n_{min}. For example, for the transfer $A_1 \rightarrow C_1$ this number is four for the INEPT-based and two for INEPT/ planar-based CTEs, respectively. In the former case, the minimal pulse-sequence length required to achieve near-optimal transfer for $n \geqslant n_{min}$ is indeed the estimated value $\Theta_{min} = 3.62$.
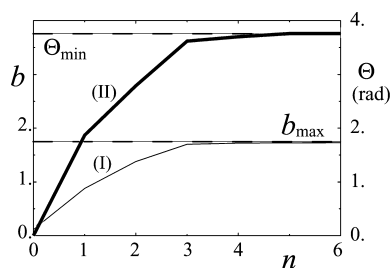

Fig. 4. Numerical estimates of the maximal achievable coherence transfer b (curve I) and corresponding minimal pulse sequence length Θ required to achieve this transfer (curve II), displayed as functions of the complexity n of the INEPT-based CTE (Fig. 1C) for the transfer $A_1 \rightarrow C_1$. For each n 10,000 unconstrained maximizations of f_{AC} (Eq. (8a)) starting with random x were performed resulting in a pool of NMR experiments each characterized by specific b and Θ. The pool was doubly sorted according to b and Θ to obtain the maximal and minimal values (curves I and II, respectively) of the corresponding parameters attained within one experiment. The theoretical unitary bound for this transfer, $b_{max} = \sqrt{3}$, is shown as a horizontal line. The estimated minimal pulse sequence length, $\Theta_{min} = 3.62$, to achieve this transfer is also shown as a horizontal line.

In the construction and optimization of CTEs, n should be kept at as low as possible since: (i) increasing the complexity above a certain point leads neither to a reduction of the transfer time nor a further increase of the transfer efficiency; (ii) the pulse sequences with large n are more sensitive to experimental errors. Note that a consistent theory accounting for the dependence of the maximal efficiency and minimal transfer time on n of CTEs remains to be developed.

3.3. Optimization of the transfer function using molecular dynamics

The search for local minima of the function $V(x)$ of Eq. (11) in the space of pulse-sequence variables x, using either a gradient-based (steepest-descent) or a molecular-dynamics (simulated-annealing) approach, was implemented in a C++ program. Because the steepest-descent algorithm only leads to the local minimum closest to a given starting point, the global minimum of V can only be located by performing a large number of minimizations initiated from random starting points. In contrast, the simulated-annealing approach with a suitably optimized protocol often permits the determination of the global minimum in a single run. A simulated-annealing protocol is defined by four parameters, namely the (common) mass assigned to the pulse-sequence variables, the initial (high) and final (low) kinetic energies, and the duration of the run. An appropriate minimal mass was determined by ensuring energy conservation (no drift, negligible fluctuations) in simulations without temperature coupling. The use of a larger mass leads to slower sampling without further improving energy conservation, and is thus not recommended. Values for the various other parameters involved in the two algorithms were optimized by trial and error (Supplementary Materials). The evolution of the kinetic (linearly decreased) and potential (function V in Eq. (11)) energies along a typical simulated-annealing run are shown in Fig. 5.

The threshold for linearization of the penalty term associated with the pulse-sequence duration (Eq. (12)) was set to $\Theta_0 = 7$ rad. The biasing parameters μ and v in Eq. (11) were varied in the ranges $\mu = 0.01$–5 rad^{-1} and $v = 10$–100 rad^{-1}. The resulting optimized CTEs were evaluated by calculation of the corresponding simulated spectra (see Fig. 2). Indicative values of $\mu = 1$ rad^{-1} and $v = 25$ rad^{-1} were found to provide a good compromise between transfer efficiency and CTE duration.

In general, pulse sequences of similar quality can also be produced using the steepest-descent algorithm. However, although simulated annealing nearly systematically reaches the global minimum in a single run, steepest descent typically requires the minimization of hundreds of random starting points before reaching this global
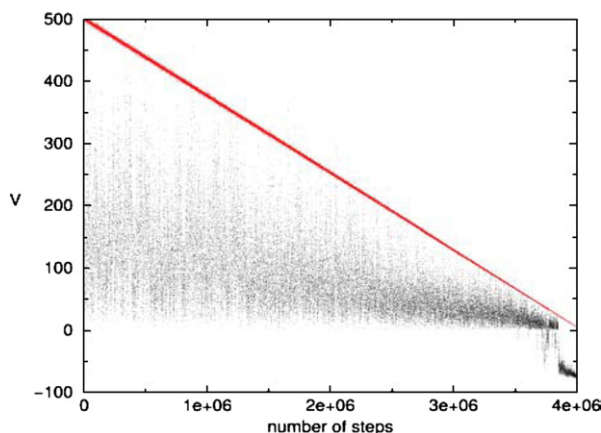
Fig. 5. Example of evolution of "kinetic" energy (straight line, gradually decreased from 500 to 5) and potential energy (Eq. (11), with $\Theta_0 = 7$ rad, $\mu = 1$ rad^{-1}, and $v = 25$ rad^{-1}) in reduced units (see Supplementary Materials) during a typical simulated-annealing optimization run. The curve corresponds to the transfer $A_2 \rightarrow C_1$, optimized with simultaneous suppression of the spurious target D_1 for an INEPT-based CTE (Fig. 1C) with $n = 4$.

minimum. For pulse sequences of limited complexity ($n \leqslant 3$), the efficiency of the two methods in terms of computer time is comparable. However, simulated annealing tends to outperform steepest descent upon increasing the complexity of the pulse sequence.

The optimization of complex pulse sequences often results in the appearance of delay lengths close to zero. For example, most of the optimized INEPT-based CTEs, with $n = 4$ or 5 could be reduced to a simpler CTE with $n = 3$ possessing similar properties. Similarly, INEPT/planar-based CTEs with $n = 4$ could generally be reduced to CTEs with $n = 2$. Note, finally, that optimized pulse sequences are often degenerate, i.e., identical values of V could often be achieved by multiple pulse sequences. In general, the degenerate sequences were characterized by similar delay lengths and pulse phase shifts differing through integer fractions of π.

As discussed previously, a CTE optimized for efficiency by direct maximization of the function f_{AC} in Eq. (8a) without additional restraints is generally characterized by spurious transitions in the spectrum, corresponding to unwanted elements in the transformation matrix. These effects are illustrated in Figs. 2B and 3C for the $A_1 \rightarrow C_1$ transfer through the optimized pulse sequence OCTE$_1$ (Table 1). Performing the optimization of an INEPT/planar-based CTE with $n = 2$ by minimizing the function V in Eq. (11) (with the suppressed matrix D_1, $\Theta_0 = 7$ rad^{-1}, $\mu = 1$ rad^{-1} and $v = 25$ rad^{-1}), i.e., including active suppression of unwanted transitions and minimization of the pulse-sequence duration, results in a "cleaner" transfer operator $UAU^\dagger$ and spectrum, without significantly compromising the high transfer efficiency for the desired transition and the short duration of the pulse sequence. This optimized

CTE will be referred to as OCTE$_2$. The corresponding vector x is given in Table 1, the matrix representation of $UAU^\dagger$ in Fig. 3C, and the simulated spectrum in Fig. 2C. A similar optimization (with the suppressed matrix D_2, and identical parameters) was performed of an INEPT-based CTE with $n = 4$ for the transfer $A_2 \rightarrow C_1$, that will be referred to as OCTE$_3$. The corresponding vector x is given in Table 1, the matrix representation of $UAU^\dagger$ in Fig. 1S in Supplementary Material, and the simulated spectrum in Fig. 2D. For the two optimized CTEs, 98 and 90% of the maximal unitary bounds are achieved (Table 1). Note that optimized INEPT/planar-based CTEs were generated for both the transfers of $A_1 \rightarrow C_1$ and $A_2 \rightarrow C_1$. However, the experimental implementation of the planar Hamiltonian of Eq. (6c) using a DIPSI-2 pulse train imposes a technical limitation on the minimal length of the individual planar-mixing elements. So far, no experimentally attractive solution based on an alternating INEPT/planar-based CTE was found for the transfer of $A_2 \rightarrow C_1$. On the other hand, INEPT-based CTEs are free from these constraints, although, they tend to produce on average somewhat longer experiments achieving the same transfer efficiency. Clearly, more ample numerical statistics as well as analytical work are needed to comparatively evaluate these two types of CTEs.

3.4. Measurements of ^1H–^1H and ^1H–^{13}C residual dipolar couplings in the methyl groups

As an illustrative application of the method, optimized CTEs are used to quantitatively measure residual ^1H–^1H (D_{HH}) and ^1H–^{13}C (D_{HC}) dipolar couplings (RDC) in a protein weakly aligned by means of Pf1 phages [48] at the optimal sensitivity using a minimal number of spectra. Two optimized CTEs were selected for this experimental implementation, OCTE$_2$ and OCTE$_3$, which correlate ^{13}C and ^1H chemical shifts in methyl groups using the pathways $A_1 \rightarrow C_1$ (complemented with $A_1 \rightarrow C_2$) and $A_2 \rightarrow C_1$ (complemented with $A_2 \rightarrow C_2$), respectively.

The performance of the newly designed experiments is demonstrated using diamagnetic heme chaperone apo-CcmE (17 kDa) [49] as a model system. Fig. 6 shows two-dimensional [^{13}C, ^1H]-correlation spectrum obtained with OCTE$_2$. At the achieved average signal-to-noise ratio of about 20, the suppressed components are below the noise level. The values and signs of the residual dipolar coupling constant D_{HH} can be easily extracted from one-dimensional ^1H-slices taken through the corresponding peaks in the spectra, as shown in Fig. 7. By repeating the measurements, the statistical variation of the obtained values of D_{HH} was estimated to be in the range of 0.4 Hz. The experiment using the pathway of $A_2 \rightarrow C_1$ appears to be preferable, considering its tolerance to differential-relaxation effects during
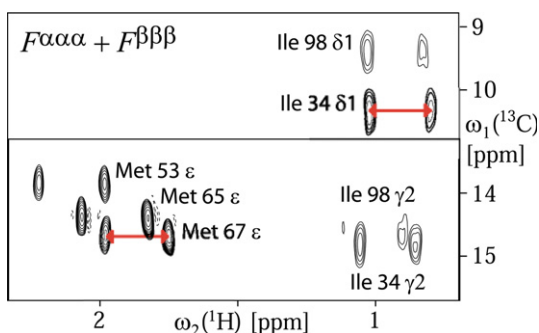
Fig. 6. Sample of the two-dimensional [^{13}C,^{1}H]-correlation spectrum selecting the C_1 components of methyl groups. The spectrum was measured using the source operator A_1 (Fig. 2A) with an INEPT-based OCTE$_2$ (Table 1) for 0.1 mM apo-CcmE in 20 mM Tris buffer (pH 7.5, $T = 298$ K) in a 10 mg/ml solution of Pf1 phages. The experiment was run on a Bruker Avance 600 spectrometer with $t_{1\,max} = 16.55$ ms and $t_{2\,max} = 106.5$ ms, an interscan delay of 1 s, 100×512 complex points resulting in an acquisition time of 6 h. The time domain data were multiplied with a cosine function in the t_1 and t_2 dimensions and zero-filled to 512 and 8192 points, respectively. Radio-frequency carrier offsets were placed at 0.5 ppm (^{1}H) and 20 ppm (^{13}C).
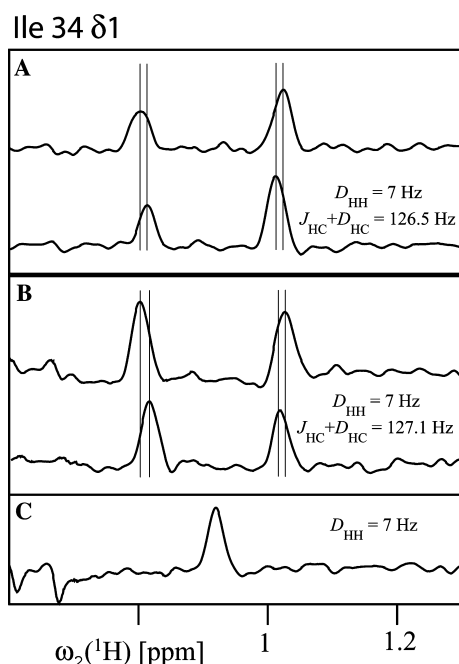

Fig. 7. One-dimensional slices along the ω_2 dimension of the 2D [^{1}H,^{13}C] correlation spectra, taken at the corresponding cross-peaks of the methyl groups $\delta 1$ of ILE34. In (A) slices are taken from the two-dimensional [^{13}C,^{1}H]-correlation spectra measured using the transfer $A_1 \rightarrow C_1$ (upper slice) and $A_1 \rightarrow C_2$ (lower slices) with OCTE$_2$ (see Table 1) and in (B) the transfer $A_2 \rightarrow C_1$ (upper slice) and $A_2 \rightarrow C_2$ (lower slices) with OCTE$_3$ (see Table 1). For comparison, the corresponding slice taken from the (H$^{\alpha\alpha}$)-selected two-dimensional [^{13}C,^{1}H]-spectrum [1] acquired in the same total experimental time is shown in (C). The extracted RDC values are shown.

the chemical shift evolution period. Note that for holo-CcmE, the proposed experiment provided values of D_{HH} which are significantly smaller than the linewidth of ^{1}H-

resonances, so that alternative methods designed to detect the individual transitions in the form of the ^{1}H antiphase magnetization would fail [15].

In summary, the use of presently developed CTE optimization algorithm permitted the construction of two new complete NMR experiments achieving maximal possible coherence transfer efficiency and nearly complete suppression of undesired signals. Both features are critical for the quantitative and unbiased determination of residual dipolar couplings in methyl groups, and the sensitivity of the present experiments is doubled as compared to that of the previous experiment [1]. A variety of other experiments can be designed using the present optimization approach. For example, the inphase-type spectra can be augmented with the corresponding antiphase spectra to reduce spectral overlap. In this case, an optimized experiment should be particularly useful in combination with isotope-labeling schemes, where the protein is perdeuterated except for the methyl groups [50,47], thereby reducing losses due to relaxation and passive scalar and dipolar couplings.

3.5. Balance between transfer efficiency and pulse sequence duration

The results of numerical CTE optimizations shown in Fig. 4 suggest that it is feasible to trade some of the transfer efficiency for a shorter pulse-sequence duration. The corresponding closed-form analytical relationships between the efficiency of the polarization (coherence) transfer and the minimal time required to achieve it are established only for a few particular types of transfers [37]. Using the present optimization method, shorter pulse sequences can be produced by imposing stronger penalties on the duration of CTE (weighting factor v in Eq. (11)). Unfortunately, however, the shorter pulse sequences are usually affected by a poorer suppression of undesired multiplet components, so that a balance between the CTE duration and artifact suppression should be maintained. If shorter CTEs with suboptimal transfer efficiencies are to be generated, an alternative to the penalty-function approach for artifact suppression (employed in the presented study) should be considered. For example, the most prominent (TROSY-enhanced) undesired central transitions of the ^{13}C-decoupled ^{1}H-triplet (Fig. 2A) can be eliminated by the appropriate choice of the heteronuclear gradient-based echo/anti-echo pathway (Fig. 2D). The previously suggested two-dimensional [^{13}C,^{1}H$^{\alpha\alpha/\beta\beta}$]^{Methyl} HSQC experiment [1] is yet another practical example of a shorter and suboptimal CTE, nonetheless delivering a comparable spectral sensitivity even for the small protein studied here (Fig. 7C). In this experiment, magnetic field gradients inserted between the constituent INEPT elements are

employed to rebalance parallel coherence transfer pathways. This approach provides an additional capability to control quantum evolution and can be used for systematic CTE design in future work.

Acknowledgments

Appendix. Supplementary material

Figure 1S showing the matrix representation associated with the coherence transfer $A_2 \rightarrow C_1$. The document "Optimization of CTEs using steepest descent or simulated annealing" providing the details of the optimization algorithms applied in the present study are presented.

Supplementary data associated with this article can be found, in the online version, at doi:10.1016/j.jmr.2004. 09.016.

References

[1] K. Pervushin, B. Vogeli, Observation of individual transitions in magnetically equivalent spin systems, J. Am. Chem. Soc. 125 (2003) 9566–9567.

[2] K. Pervushin, R. Riek, G. Wider, K. Wuthrich, Attenuated T-2 relaxation by mutual cancellation of dipole- dipole coupling and chemical shift anisotropy indicates an avenue to NMR structures of very large biological macromolecules in solution, Proc. Natl. Acad. Sci. USA 94 (1997) 12366–12371.

[3] J.E. Ollerenshaw, V. Tugarinov, L.E. Kay, Methyl TROSY: explanation and experimental verification, Magn. Reson. Chem. 41 (2003) 843–852.

[4] V. Tugarinov, P.M. Hwang, J.E. Ollerenshaw, L.E. Kay, Cross-correlated relaxation enhanced H-1-C-13 NMR spectroscopy of methyl groups in very high molecular weight proteins and protein complexes, J. Am. Chem. Soc. 125 (2003) 10420–10428.

[5] V. Tugarinov, R. Sprangers, L.E. Kay, Line narrowing in methyl-TROSY using zero-quantum H-1-C-13 NMR spectroscopy, J. Am. Chem. Soc. 126 (2004) 4921–4925.

[6] D.M. Korzhnev, K. Kloiber, V. Kanelis, V. Tugarinov, L.E. Kay, Probing slow dynamics in high molecular weight proteins by methyl-TROSY NMR spectroscopy: application to a 723-residue enzyme, J. Am. Chem. Soc. 126 (2004) 3964–3973.

[7] I. Bertini, C. Luchinat, D. Tarchi, Are true scalar proton proton connectivities ever measured in cosy spectra of paramagnetic macromolecules, Chem. Phys. Lett. 203 (1993) 445–449.

[8] J. Qin, F. Delaglio, G.N. Lamar, A. Bax, Distinguishing the effects of cross-correlation and *J*-coupling in Cosy spectra of paramagnetic proteins, J. Magn. Reson. Ser. B 102 (1993) 332–336.

[9] R. Ghose, J.H. Prestegard, Electron spin-nuclear spin cross-correlation effects on multiplet splittings in paramagnetic proteins, J. Magn. Reson. 128 (1997) 138–143.

[10] J. Boisbouvier, P. Gans, M. Blackledge, B. Brutscher, D. Marion, Long-range structural information in NMR studies of paramagnetic molecules from electron spin-nuclear spin cross-correlated relaxation, J. Am. Chem. Soc. 121 (1999) 7700–7701.

[11] P.K. Mandal, P.K. Madhu, N. Muller, Nuclear magnetic relaxation of methyl protons in a paramagnetic protein: cross-correlation effects, Chem. Phys. Lett. 32 (2000) 269–276.

[12] I. Bertini, J. Kowalewski, C. Luchinat, G. Parigi, Cross correlation between the dipole–dipole interaction and the curie spin relaxation: the effect of anisotropic magnetic susceptibility, J. Magn. Reson. 152 (2001) 103–108.

[13] I. Bertini, G. Cavallaro, M. Cosenza, R. Kummerle, C. Luchinat, M. Piccioli, L. Poggi, Cross correlation rates between Curie spin and dipole–dipole relaxation in paramagnetic proteins: the case of cerium substituted calbindin D-9k, J. Biomol. NMR 23 (2002) 115–125.

[14] P.K. Madhu, P.K. Mandal, N. Muller, Cross-correlation effects involving Curie spin relaxation in methyl groups, J. Magn. Reson. 155 (2002) 29–38.

[15] A. Kaikkonen, G. Otting, Residual dipolar H-1–H-1 couplings of methyl groups in weakly aligned proteins, J. Am. Chem. Soc. 123 (2001) 1770–1771.

[16] G. Kontaxis, A. Bax, Multiplet component separation for measurement of methyl C-13–H-1 dipolar couplings in weakly aligned proteins, J. Biomol. NMR 20 (2001) 77–82.

[17] N. Sibille, B. Bersch, J. Coves, M. Blackledge, B. Brutscher, Side chain orientation from methyl H-1–H-1 residual dipolar couplings measured in highly deuterated proteins, J. Am. Chem. Soc. 124 (2002) 14616–14625.

[18] J.R. Tolman, J.M. Flanagan, M.A. Kennedy, J.H. Prestegard, Nuclear magnetic dipole interactions in field-oriented proteins—information for structure determination in solution, Proc. Natl. Acad. Sci. USA 92 (1995) 9279–9283.

[19] N. Tjandra, A. Bax, Direct measurement of distances and angles in biomolecules by NMR in a dilute liquid crystalline medium, Science 278 (1997) 1111–1114.

[20] N. Tjandra, J.G. Omichinski, A.M. Gronenborn, G.M. Clore, A. Bax, Use of dipolar 1H–15N and 1H–13C couplings in the structure determination of magnetically oriented macromolecules in solution, Nat. Struct. Biol. 4 (1997) 732–738.

[21] R.R. Ernst, G. Bodenhausen, A. Wokaun, The Principles of Nuclear Magnetic Resonance in One and Two Dimensions, Clarendon Press, Oxford, 1987.

[22] J. Cavanagh, W.J. Fairbrother, A.G. Palmer, N.J. Skelton, Protein NMR Spectroscopy: Principles and Practice, Academic Press, New York, 1996.

[23] T. Schulte-Herbruggen, T.S. Untidt, N.C. Nielsen, O.W. Sorensen, Broadband composite spin-state-selective rotations for NMR spectroscopy on partially aligned molecules, J. Chem. Phys. 115 (2001) 8506–8517.

[24] N. Khaneja, B. Luy, S.J. Glaser, Boundary of quantum evolution under decoherence, Proc. Natl. Acad. Sci. USA 100 (2003) 13162–13166.

[25] N. Khaneja, T. Reiss, B. Luy, S.J. Glaser, Optimal control of spin dynamics in the presence of relaxation, J. Magn. Reson. 162 (2003) 311–319.

[26] J. Cavanagh, A.G. Palmer, P.E. Wright, M. Rance, Sensitivity improvement in proton-detected 2-dimensional heteronuclear relay spectroscopy, J. Magn. Reson. 91 (1991) 429–436.

[27] G. Barbato, M. Ikura, L.E. Kay, R.W. Pastor, A. Bax, Backbone dynamics of calmodulin studied by N-15 relaxation using inverse detected 2-dimensional NMR-spectroscopy—the central helix is flexible, Biochemistry 31 (1992) 5269–5278.

[28] J. Schleucher, M. Schwendinger, M. Sattler, P. Schmidt, O. Schedletzky, S.J. Glaser, O.W. Sorensen, C. Griesinger, A general enhancement scheme in heteronuclear multidimensional nmr employing pulsed-field gradients, J. Biomol. NMR 4 (1994) 301–306.

[29] M. Sattler, P. Schmidt, J. Schleucher, O. Schedletzky, S.J. Glaser, C. Griesinger, Novel pulse sequences with sensitivity enhancement for in-phase coherence transfer employing pulsed-field gradients, J. Magn. Reson. Ser. B 108 (1995) 235–242.

[30] K. Pervushin, G. Wider, K. Wuthrich, Single transition-to-single transition polarization transfer (ST2-PT) in [N-15, H-1]-TROSY, J. Biomol. NMR 12 (1998) 345–348.

[31] T. Untidt, T. Schulte-Herbruggen, B. Luy, S.J. Glaser, C. Griesinger, O.W. Sorensen, N.C. Nielsen, Design of NMR pulse experiments with optimum sensitivity: coherence-order-selective transfer in I2S and I3S spin systems, Mol. Phys. 95 (1998) 787–796.

[32] J. Stoustrup, O. Schedletzky, S.J. Glaser, C. Griesinger, N.C. Nielsen, O.W. Sorensen, Generalized bound on quantum dynamics—efficiency of unitary transformations between non-Hermitian states, Phys. Rev. Lett. 74 (1995) 2921–2924.

[33] S.J. Glaser, T. Schulte-Herbruggen, M. Sieveking, O. Schedletzky, N.C. Nielsen, O.W. Sorensen, C. Griesinger, Unitary control in quantum ensembles: maximizing signal intensity in coherent spectroscopy, Science 280 (1998) 421–424.

[34] T.S. Untidt, S.J. Glaser, C. Griesinger, N.C. Nielsen, Unitary bounds and controllability of quantum evolution in NMR spectroscopy, Mol. Phys. 96 (1999) 1739–1744.

[35] N. Khaneja, R. Brockett, S.J. Glaser, Time optimal control in spin systems, Phys. Rev. A 63, art. no.-032308 (2001).

[36] N. Khaneja, S.J. Glaser, R. Brockett, Sub-Riemannian geometry and time optimal control of three spin systems: quantum gates and coherence transfer, Phys. Rev. A 65, art. no.-032301 (2002).

[37] T.O. Reiss, N. Khaneja, S.J. Glaser, Time-optimal coherence-order-selective transfer of in-phase coherence in heteronuclear IS spin systems, J. Magn. Reson. 154 (2002) 192–195.

[38] W.F. Vangunsteren, H.J.C. Berendsen, Computer-simulation of molecular-dynamics—methodology, applications, and perspectives in chemistry, Angew. Chem.-Int. Edit. Engl. 29 (1990) 992–1023.

[39] S. Kirkpatrick, C.D. Gelatt, M.P. Vecchi, Optimization by simulated annealing, Science 220 (1983) 671–680.

[40] N.C. Nielsen, T. Schulteherbruggen, O.W. Sorensen, Bounds on spin dynamics tightened by permutation symmetry—application to coherence transfer in I2s and I3s spin systems, Mol. Phys. 85 (1995) 1205–1216.

[41] N.C. Nielsen, O.W. Sorensen, Conditional bounds on polarization transfer, J. Magn. Reson. Ser. A 114 (1995) 24–31.

[42] T.S. Untidt, T. Schulte-Herbruggen, O.W. Sorensen, N.C. Nielsen, Nuclear magnetic resonance coherence-order- and spin-state-selective correlation in I2S spin systems, J. Phys. Chem. A 103 (1999) 8921–8926.

[43] L. Muller, Sensitivity enhanced detection of weak nuclei using heteronuclear multiple quantum coherence, J. Am. Chem. Soc. 101 (1979) 4481–4484.

[44] G. Bodenhausen, D.J. Ruben, Natural abundance nitrogen-15 NMR by enhanced heteronuclear spectroscopy, Chem. Phys. Lett. 69 (1980) 185–189.

[45] M.H. Levitt, The signs of frequencies and phases in NMR, J. Magn. Reson. 126 (1997) 164–182.

[46] G.A. Morris, R. Freeman, J. Am. Chem. Soc. 101 (1979) 760–762.

[47] V. Tugarinov, L.E. Kay, An isotope labeling strategy for methyl TROSY spectroscopy, J. Biomol. NMR 28 (2004) 165–172.

[48] M.R. Hansen, L. Mueller, A. Pardi, Tunable alignment of macromolecules by filamentous phage yields dipolar coupling interactions, Nat. Struct. Biol. 5 (1998) 1065–1074.

[49] E. Enggist, L. Thony-Meyer, P. Guntert, K. Pervushin, NMR structure of the heme chaperone CcmE reveals a novel functional motif, Structure (2002).

[50] M.K. Rosen, K.H. Gardner, R.C. Willis, W.E. Parris, T. Pawson, L.E. Kay, Selective methyl group protonation of perdeuterated proteins, J. Mol. Biol. 263 (1996) 627–636.

[51] L.E. Kay, P. Keifer, T. Saarinen, Pure absorption gradient enhanced heteronuclear single quantum correlation spectroscopy with improved sensitivity, J. Am. Chem. Soc. 114 (1992) 10663–10665.